Nanoscale

PAPER

View Article Online
View Journal | View Issue

Cite this: *Nanoscale*, 2018, **10**, 13986

Spontaneous valley splitting and valley pseudospin field effect transistors of monolayer $VAgP_2Se_6$

Zhigang Song, †[a,b] Xiaotian Sun, †[c] Jiaxin Zheng,[d] Feng Pan,[d] Yanglong Hou,[e] Man-Hong Yung,*[b] Jinbo Yang*[a,f,g] and Jing Lu*[a,g]

Received 25th May 2018,
Accepted 22nd June 2018

DOI: 10.1039/c8nr04253e

rsc.li/nanoscale

Valleytronics has attracted much attention due to its potential applications in the information processing industry. Creation of permanent valley polarization (PVP), *i.e.* unbalanced occupation at different valleys, is a vital requirement for practical devices in valleytronics. However, the development of an appropriate material with PVP remains a main challenge. Here we used first-principles calculations to predict that the spin–orbit coupling and magnetic ordering allow spontaneous valley Zeeman-type splitting in the pristine monolayer of $VAgP_2Se_6$. After suitable doping of $VAgP_2Se_6$, the Zeeman-type valley splitting results in a PVP, similar to the effect of spin polarization in spintronics. The $VAgP_2Se_6$ monolayer has nonequivalent valleys which can emit or absorb circularly polarized photons with opposite chirality. It thus shows great potential to be used as a photonic chirality filter and a circularly polarized light source. We then designed a valley pseudospin field effect transistor (VPFET) based on the monolayer $VAgP_2Se_6$, akin to the spin field effect transistors. In contrast to the current common transistors, VPFETs carry information of not only the electrons but also the valley pseudospins, far beyond common transistors.

In some two-dimensional (2D) semiconductors, the valence band maximum (VBM) and the conduction band minimum (CBM) are not at an equivalent momentum position in the reciprocal space. These band edges are named valleys, and the carriers occupying these valleys exist as self-rotating wave packets expanding over different unit cells in the real space. The wave packets at different valleys have an opposite rotation direction (see Fig. 1(a)). The rotating wave packets are quasi-particles with chirality. The chirality of valleys leads to a lot of interesting phenomena, such as circular dichroism, the valley Hall effect and valley orbital magnetism.[1–3] Besides, different valleys can be controlled separately. The technology of control and application of valleys forms the basis of valleytronics.

As a new degree of freedom, valleys have attracted immense attention due to their quantum phenomena[4] and their potential applications in the information processing industry.[5–8] The valley polarization can be realized in the monolayer (ML) MoS_2 by circularly polarized optical excitation. When it is created by circularly polarized optical excitation, the valley polarization is dynamical. The lifespan of valley carriers (approximately a few picoseconds) is thus too short to be utilized.[6,7,9] Therefore, the generation of permanent valley polarization (PVP) becomes a central theme and an urgent problem to be solved in the valleytronics.[10] PVP may offer an opportunity to realize stable valleytronic devices such as nonvolatile random access memories based on valleys and to reproduce some phenomena locked by time reversal symmetry, such as valley filtering, circularly polarized electroluminescence, and the anomalous Hall effect.[11] PVP can be generated by suitable doping after lifting valley degeneracy, which results in Zeeman-type valley splitting in analogy to spin Zeeman splitting.

Recently, several external methods such as applying a magnetic field or electric field,[12] optical Stark effect,[13] magnetic impurities, and magnetic substrates[14] have been utilized to achieve Zeeman-type valley splitting.[15,16] However, the valley degeneracy is restored and valley polarization is quenched after the external fields or substrates are removed. From a practical perspective, the required field to achieve a sizable valley

[a]*State Key Laboratory for Mesoscopic Physics and School of Physics, Peking University, Beijing 100871, P. R. China. E-mail: Jbyang@pku.edu.cn, Jinglu@pku.edu.cn*
[b]*Institute for Quantum Science and Engineering and Department of Physics, South University of Science and Technology of China, Shenzhen 518055, China. E-mail: Yung@sustc.edu.cn*
[c]*College of Chemistry and Chemical Engineering, and Henan Key Laboratory of Function-Oriented Porous Materials, Luoyang Normal University, Luoyang 471934, P. R. China*
[d]*School of Advanced Materials, Peking University, Shenzhen Graduate School, Shenzhen 518055, People's Republic of China*
[e]*Department of Materials Science and Engineering, College of Engineering, Peking University, Beijing 100871, China*
[f]*Beijing Key Laboratory for Magnetoelectric Materials and Devices, Beijing 100871, P. R. China*
[g]*Collaborative Innovation Center of Quantum Matter, Beijing 100871, P. R. China*
†These authors equally contribute to this work.

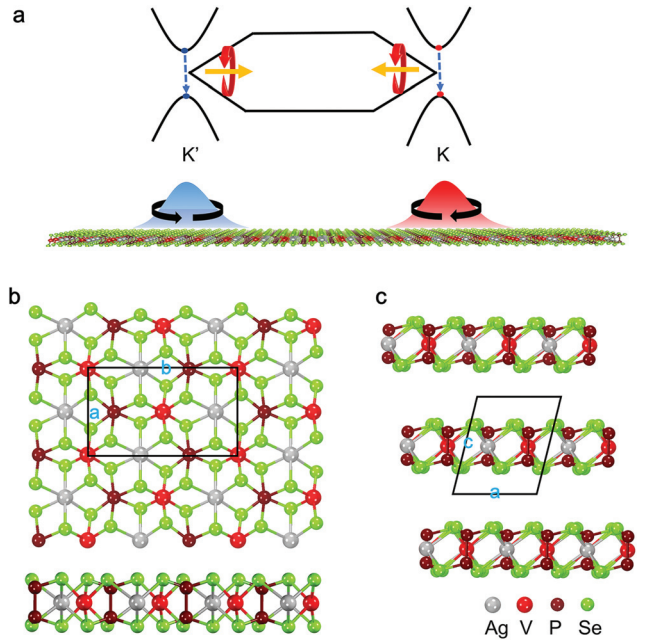

Fig. 1 Crystal structure of $VAgP_2Se_6$. (a) Schematic of the self-rotating valley wave packets for different valleys (K and K′ points) in the real space. The red and blue colors represent the left- and right-chiral wave packets, respectively. (b) Top (upper) and side (lower) views of monolayer $VAgP_2Se_6$. (c) Side view of bulk $VAgP_2Se_6$ by layer stacking. The outlines of the monolayer and bulk unit cells are sketched by black lines.

Zeeman-type splitting is difficult to realize and unbeneficial to the future integrated circuits of valleytronic devices. Magnetic impurities or substrates usually have a negative impact on the electron occupation of 2D valleytronic materials due to charge transfer or doping.[17,18] It is thus highly desirable to explore internal (spontaneous) valley polarization (namely valley ferromagnetism[19]). Up to now, spontaneous valley polarization has not been found except that the monolayer (ML) VSe_2 was predicted to have this property.[20,21] However, the entangled spins in the vicinity of the Fermi level prevented ML VSe_2 from being observed.

In this article, we predict that a narrow-bandgap ferromagnetic semiconductor, ML $VAgP_2Se_6$, has a pair of single-spin massive Dirac cones. This pair of massive Dirac cones constitutes a binary valley degree of freedom in a rectangular cell, which is different from the common honeycomb lattices in valleytronics. The valleys are spontaneously nondegenerate due to spin–orbit coupling (SOC) and intrinsic ferromagnetism. The spontaneous valley splitting and pristine stoichiometry promise convenient fabrication of valleytronic devices. Based on the optical selection rule, ML $VAgP_2Se_6$ can work as a photonic chirality filter in the terahertz region and an ultrathin circularly-polarized-laser, which are long-sought in optics. We further design a transistor based on this valleytronic material and name it the valley pseudospin field effect transistor (VPFET), in analogy to the spin field effect transistor. The valley current in ML $VAgP_2Se_6$ is tunable under suitable bias voltages (V_{ds}) and gate voltages (V_g). The chirality characterized by Berry curvature can be detected by micro optical Kerr rotation or optical polarization of luminescence. VPFET is a type of multifunctional devices beyond common transistors by chirality. The pseudospin field transistors can be treated as the third member of the transistor family in addition to the electronic transistor and spin transistor. All work here, especially the simulation of the devices, is performed by first-principles calculations of a stable two-dimensional material and thus within the reach of the current experiments.

The main novelty of the current results is as follows: we predict a previously unknown ferromagnetic two-dimensional semiconductor. We find a spontaneous valley Zeeman-type splitting in the pristine monolayer $VAgP_2Se_6$, which is similar to spin polarization. Valley pseudospin Zeeman splitting is an unknown permanent valley polarization. The valley permanent polarization is a critical step to realize valleytronic devices. Based on valley Zeeman-type splitting, new-functional devices with the reach of current experiments, especially valley pseudospin transistors, are designed and simulated by the first-principles calculations. The valley pseudospin with spontaneous polarization thus provides a platform for future valleytronic devices in analogy to spintronic devices, such as tunneling field effect transistors (TFETs) and metal–oxide-semiconductor field effect transistors (MOSFETs) based on valleys. Besides the electronic transistors and spin transistors, the pseudospin field transistors are the third kind in the transistor family. Altogether, our work may open an avenue toward the low-power and high-performance valleytronic devices in the future.

Results and discussion

Spontaneous valley splitting

Bulk $VAgP_2Se_6$ is stacked with layers consisting of V and Ag atoms and diatomic P, centering at the rings of six Se atoms (see Fig. 1(b and c)).[22] The neighboring P diatoms, V and Ag atoms are bridged through two Se atoms. The equilibrium lattice constants observed by X-ray powder diffraction are a = 6.34 Å, b = 11.18 Å, and c = 6.98 Å, respectively. The interlayers are bonded *via* weak van der Waals interaction with an interlayer distance of 3.26 Å, allowing layers to be exfoliated. Bulk $VAgP_2Se_6$ is a ferromagnetic half-metal with a measured Curie temperature of 29 K.[22] Both bulk and ML have the same space group of C_2.

The calculated energy difference between ferromagnetic and possible antiferromagnetic states indicates that the ferromagnetic state is the most stable state. The total energy of the ferromagnetic state is 126 meV per unit cell lower than that of the antiferromagnetic state where the nearest neighboring spins are opposite. The method to determine the magnetic ordering is similar to the one previously reported.[23–27] The ferromagnetic state of ML $VAgP_2Se_6$ is an insulator with a magnetic moment of 4 μ_B per unit cell. According to the Mermin–Wagner no-go theorem, the long-range ferromagnetism in 2D systems can be easily destroyed by thermal fluctuations;

however, these thermal fluctuations can be counteracted by magnetic anisotropy. The magnetic anisotropy may give rise to a long-range ferromagnetic ordering at finite (non-zero) temperatures.[28] Actually, ferromagnetism has been predicted in the ML CrI_3 and $CrGeTe_3$,[28–30] and then an atomically thin ferromagnet was observed. The calculated magnetocrystalline energy in the ML $VAgP_2Se_6$ is approximately 1.5 meV per unit cell. The easy magnetization axis lies vertical to the layer surface. Thus, the calculated magnetocrystalline anisotropy in the $VAgP_2Se_6$ ML and the observed ferromagnetism in bulk $VAgP_2Se_6$ support the possible stable ferromagnetism in the ML $VAgP_2Se_6$.

Fig. 2(a) shows the spin-polarized band structure of ML $VAgP_2Se_6$ without SOC. The bands of majority-spin (red lines) and minority-spin (blue lines) are well split by exchange interaction. The 3d shell of the V atom is partially filled, leaving 2 unfilled d-orbits in majority-spin. The bands close to the Fermi level are dominated by majority-spin and featured by two massive Dirac cones with a bandgap of approximately 39 meV, which holds a binary degree of freedom in analogy to the electron spin. The two valleys are degenerate without including SOC, although the spin polarized bands are time-reversal asymmetric. After SOC is included, the corresponding dispersion relationship is shown in Fig. 2(b), and the valleys are nondegenerate. SOC decreases the gap of one valley to 29 meV and increases the gap of the other valley to 44 meV, forming the fundamental bandgap. The two valleys center on the line of N′–Γ–N and are labeled as K $(0, 0.267\pi)$ and K′ $(0, -0.267\pi)$, respectively (see Fig. 2(c)). The global bandgap remains a large value of 29 meV, which is a complex effect of crystal symmetry breaking and SOC. Using the approximation of the atomic orbital, the SOC can be written as $\lambda L{\cdot}S$. The orbital momentum is dominated by the component outside the basal plane, and the SOC is simplified as $\lambda L_z S_z$. In two opposite valleys, the orbital momentum, in particular the component vertical to the surface plane, has opposite signs according to Fig. 2(d and e), and the spin has the same signs according to the discussions above. Thus, the local gaps respond to the SOC in an opposite way, leading to valley Zeeman-type splitting. The component of in-plane SOC contributes to a shift of valleys in the two-dimensional momentum space.

In $S = 1/2$ systems, the Hamiltonian in the S_z basis is in the format as follows: $H = \begin{pmatrix} H_0^{\uparrow} + M_z & \\ & H_0^{\downarrow} - M_z \end{pmatrix} + \lambda(L_+S_+ + L_-S_- + L_zS_z)$, where M_z is Zeeman energy. The time-reversal operation is $T = i\sigma_y K$, where σ_y is the second spin Pauli matrix and K is the complex conjugate. The Zeeman energy results in a spin splitting and breaks the time reversal symmetry. The Zeeman energy is usually treated as a constant.[31,32] Without spin-orbital coupling, the majority-spin and minority-spin bands are independent. Single-spin-polarized bands $H_0^{\uparrow} + M_z$ or $H_0^{\downarrow} - M_z$ can be treated separately in the low-power limit near the Fermi level. If the bands are well separated, single-band approximation works well. In single-band systems, the operation $T = K$ is also a symmetry similar to the time-reversal symmetry. A single-band Hamiltonian is Hermitian and has such a one-dimensional symmetry $T = K$. Thus, the two valleys are degenerate

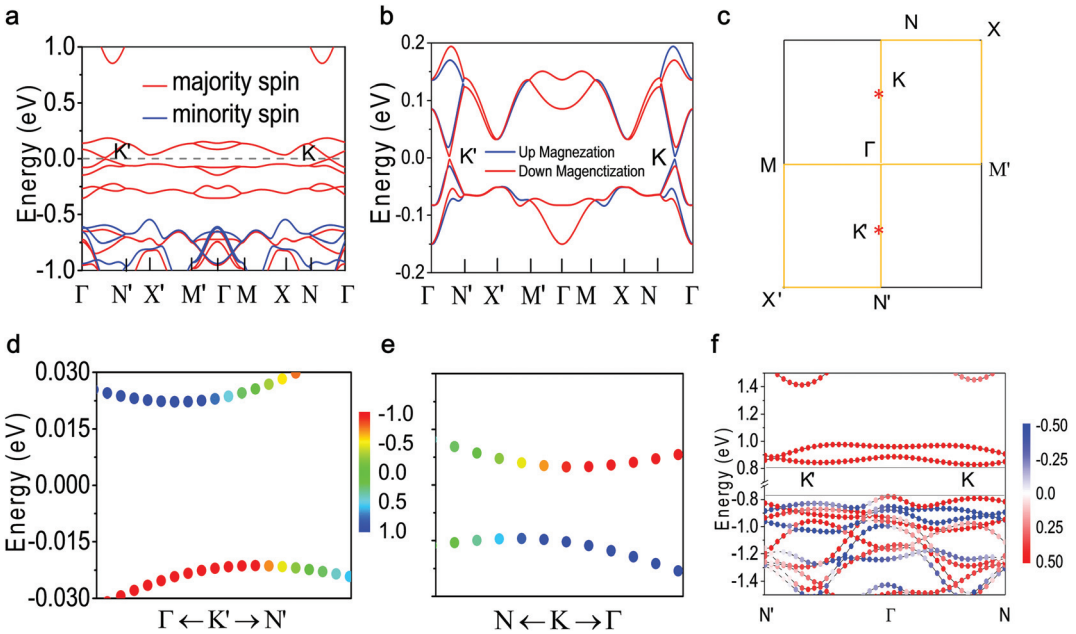

Fig. 2 Electronic structure of the monolayer $VAgP_2Se_6$. (a) Spin polarized band structure without SOC. The band structure in the vicinity of the Fermi level is fully spin polarized. (b) Comparison between band structures when the magnetization is orientated in the up and down directions. (c) Rectangular Brillouin zone and high-symmetry path colored with orange. (d, e) Zoom in of the two valleys colored by the component outside the plane of the orbital momentum. (f) Band structure calculated using HSE06 with the inclusion of SOC. The color indicates the weight of spin projection. The red and blue colors represent the spin-up and spin-down states, respectively. The Fermi level is set to zero.

according to the hidden symmetry. Indeed, the two valleys are degenerate without spin-orbital coupling in our spin-polarized calculations. The valley Zeeman-type splitting can only be realized in the systems with heavy elements, which can generate a strong spin-orbital coupling. Valley Zeeman-type splitting in the systems with light elements, such as the honeycomb BN and graphene monolayers, can be neglected even if both the inversion symmetry and the time reversal symmetry are broken.

Since the conduction band minima at the two valleys are nondegenerate, the scattering of electrons from the low-energy valley to the high-energy valley in the conduction band is forbidden at low temperature according to energy conservation, implying a very long relaxation time and a long average free path for the valley carriers. Therefore, we believe that this kind of material has a real permanent valley polarization. Although the phonon may cause an intervalley scattering at a higher temperature, these two valleys are well separated in the momentum space, and thus the intervalley scattering possibility remains small. The estimated lifetime is longer than that of the nonmagnetic valleytronic materials (10 ps),[33–35] and the estimated mean free path is longer than 10 μm based on the Fermi velocity. The long mean free path benefits from the linear dispersion of Dirac cones.

Regarding the valley contrast physics discussed below, Berry curvature ($\Omega_n(k)$) is one of the key quantities. The integrated Berry curvature in a certain zone (D) is proportional to the Hall conductance

$$\sigma_{xy} = \frac{e^2}{2\pi h}\sum_n \int_D \Omega_n(k)\mathrm{d}^2k \quad (1)$$

where the sum spans over all occupied states. e is the elementary charge of an electron and h is the Planck constant. According to Fig. 3(a), the calculated Berry curvature is valley-specific. Berry curvature plays a similar role to a Lorentz force in the presence of an in-plane electric field, resulting in a spatial separation of the carriers at opposite valleys. This is the valley Hall effect and it can be accompanied by a transverse valley current without an electron current. Berry curvature can thus be directly observed in bulk through subtle signatures of the valley Hall effect. If valleys are well separated, the valley index ($\tau = \pm$) is a good quantum number akin to the spin index. The valley Hall conductivity is defined as

$$\sigma_{xy}^{v} = \sum_\tau \sum_n \frac{e^2}{2\pi h}\int_\tau \tau\Omega_n(k)\mathrm{d}^2k \quad (2)$$

where the sum is over all the occupied states. It characterizes the transverse valley current in the presence of an in-plane electric field. The Berry curvature associated with the Kohn–Sham Bloch waves is displayed in Fig. 3(a). If suitably doped, the integration zone can cover only one valley, and the valley Hall effect is equivalent to the anomalous Hall effect. An anomalous Hall effect can be observed by tuning the Fermi level.

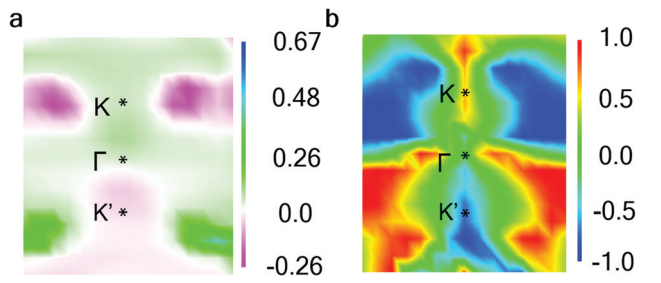

Fig. 3 Valley selectivity of the monolayer $VAgP_2Se_6$ in the Brillouin zone. (a) Momentum resolved Kohn–Sham Berry curvature of the whole occupied wave function. (b) Degree of optical circular polarization.

Device design

Generally, the different valleys absorb or emit photons with opposite chirality. The rectangular colored map in Fig. 3(b) shows the k-resolved degree of circular polarization distributed in the Brillouin zone. The k-resolved degree of circular polarization is defined as[3]

$$\eta(k) = \frac{|p_+(k)|^2 - |p_-(k)|^2}{|p_+(k)|^2 + |p_+(k)|^2} \quad (3)$$

where $P_\pm = P_x \pm iP_y$, P_α, is the canonical momentum transition matrix element connecting the valence and conduction bands. The circular polarization is selective at different valleys, and $\eta(k) \approx \pm 100\%$ for the K and K′ valleys, respectively. This implies that a left-hand (or right-hand) polarized photon is selectively absorbed in the K (K′) valley, while the opposite-chirality photon is almost prohibited.

If a beam of light in the energy window between the band-gaps of two valleys irradiates ML $VAgP_2Se_6$, only photons with certain chirality are absorbed, and the photons with the opposite spin propagate without any barriers (see Fig. 4(a)). When the magnetization is reversed, the chirality of the absorbed and transmitted photons is reversed at the same time (see Fig. 2(b)). Due to nonequivalent absorption of specific photons, this material can work as a photonic chirality filter in a certain energy interval. The absorption rate of conventional materials is usually very low, leading to a low polarization of photonic chirality. The absorption rate of 2D materials increases with the number of layers. The circular polarization of photons thus increases with the number of layers.

Advanced nanotechnology enables the fabrication of the transistors using ML $VAgP_2Se_6$. Firstly, a device of the MOSFET (illustrated in Fig. 4(b)) can be designed, which is easy to realize in current experiments.[36,37] We refer to it as the valley pseudospin field effect transistor (VPFET). A double gate is utilized. The gates are realized by a metal layer and a dielectric region of Al_2O_3 with an equivalent oxide thickness of 0.2 nm. The transports are parallel to the C_2 axis (b-direction shown in Fig. 1(a)) of the ML $VAgP_2Se_6$. The transport properties perpendicular to the C_2 axis (a-axis in Fig. 1(a)) are trivial for valleys, since the valleys merge in this direction. The atomically thin $VAgP_2Se_6$ doped with electrons are used as source and drain

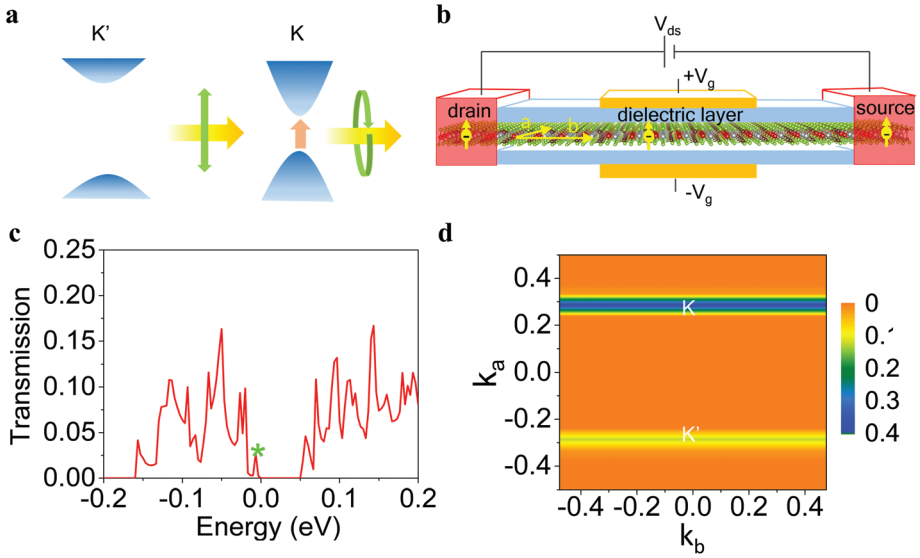

Fig. 4 Devices of the monolayer $VAgP_2Se_6$. (a) Schematic of the photonic chirality filter. (b) Schematic of the valley pseudospin metal–oxide-semiconductor field effect transistor. Arrows on the balls index the valley pseudospin. (c) Zero-bias and zero-gate-voltage transmission spectrum (spin is fully polarized) in monolayer $VAgP_2Se_6$ with SOC. (d) *k*-Resolved transmission coefficient of the state at the energy of −6.5 meV, which is labeled by the green star in the transmission spectrum.

electrodes. Without loss of generality, we use a channel that is as long as possible (up to 6.7 nm) considering our computation capacity. In accordance with the band structure, there is a small bandgap of approximately 32 meV in the transmission spectrum without any bias or gate voltages at low temperatures. This is due to the presence of a nonzero gap of the channel material (see Fig. 4(c)). The small discrepancy between the transmission gap and the bandgap (29 meV *vs.* 32 meV) is ascribed to the quantum limit effect originating from the finite channel length. The transmission coefficients near the VBM and the CBM are dominantly contributed from one valley. The *k*-resolved transmission coefficient of one energy point near the VBM (E = −6.5 meV) is shown in Fig. 4(d). According to Fig. 4(d), only one valley can be transmitted at this energy and the other is forbidden to some degree. We define a valley polarization of the transmission coefficient at one energy point $\xi(E, V_{ds}, V_g)$ as:

$$\xi(E, V_{ds}, V_g) = \frac{\int_{l+} T_+(E, V_{ds}, V_g, k_a)\mathrm{d}k_a - \int_{l-} T_+(E, V_{ds}, V_g, k_a)\mathrm{d}k_a}{\int_{l+} T_+(E, V_{ds}, V_g, k_a)\mathrm{d}k_a + \int_{l-} T_+(E, V_{ds}, V_g, k_a)\mathrm{d}k_a} \quad (4)$$

where T_+ and T_- are transmission coefficients contributed from the K and K′ points, respectively, at a given energy E, wave vector k_a, bias voltage V_{ds} and gate voltage V_g. The integral intervals l_+, and l_- are limited to the vicinity of the K and K′ points, respectively. The current between the source and drain is obtained by the modified Landauer–Bűttiker formula:

$$I(V_{ds}, V_g) = \frac{2e}{h}\int_{-\infty}^{+\infty}\int_{-\frac{\pi}{a}}^{\frac{\pi}{a}}\{T(E, V_{ds}, V_g, k_a)[f_s(E-\mu_s) - f_d(E-\mu_d)]\}\mathrm{d}k_a\mathrm{d}E \quad (5)$$

where $T(E, V_{ds}, V_g)$ is the transmission coefficient at the given energy E, wave vector k_a along the a-direction, bias voltage V_{ds} and gate voltage V_g. f is the Fermi–Dirac distribution function and μ_s and μ_d are the chemical potential of the source and drain, respectively. The temperature of 1 K is used in the source and drain. The valley polarization of the current $\zeta(I, V_{ds}, V_g)$ can be calculated by

$$\zeta(V_{ds}, V_g) = \frac{2e}{h}\sum_{\tau}\int_{-\infty}^{+\infty}\int_{l}\{\tau T_\tau(E, V_{ds}, V_g, k_a)[f_s(E-\mu_s) - f_d(E-\mu_d)]\}\mathrm{d}k_a\mathrm{d}E/I(V_{ds}, V_g) \quad (6)$$

where the integral interval (l) is limited to the vicinity of the valleys in that τ remains a good quantum number. At a small V_{ds}, $\zeta(V_{ds}, V_g) \approx \xi(E, V_{ds}, V_g)$. The valley polarization ξ of the transmission coefficient is about 51% at E = −6.5 meV. If a long channel is utilized, the quantum limit effect is very weak, and the valley polarization of the transmission coefficient is expected to be larger, even up to ξ = 100% near the Fermi level.

The principle of the VPFETs is similar to the common transistors in electronics. A bias voltage V_{ds} lifts the chemical potentials of left and right electrodes upward and downward $V_{ds}/2$, resulting in a bias window. The gate voltage V_g results in a lift of the chemical potential in the part of the gate zone. The chemical potential still resides in the bandgap under a small bias voltage of V_{ds} and a gate voltage V_g = 0. The valley transmission wave function in the real space is constrained near the source (drain) and hardly reaches the drain (source). This leads to a very low current and sets the device to an off-state. Fig. 5 displays the transmission characteristics under a small bias voltage of V_{ds} = 0.02 V. The transmitted current is 1.97×10^{-4} μA μm^{-1} under V_{ds} = 0.02 V and V_g = 0 V. According

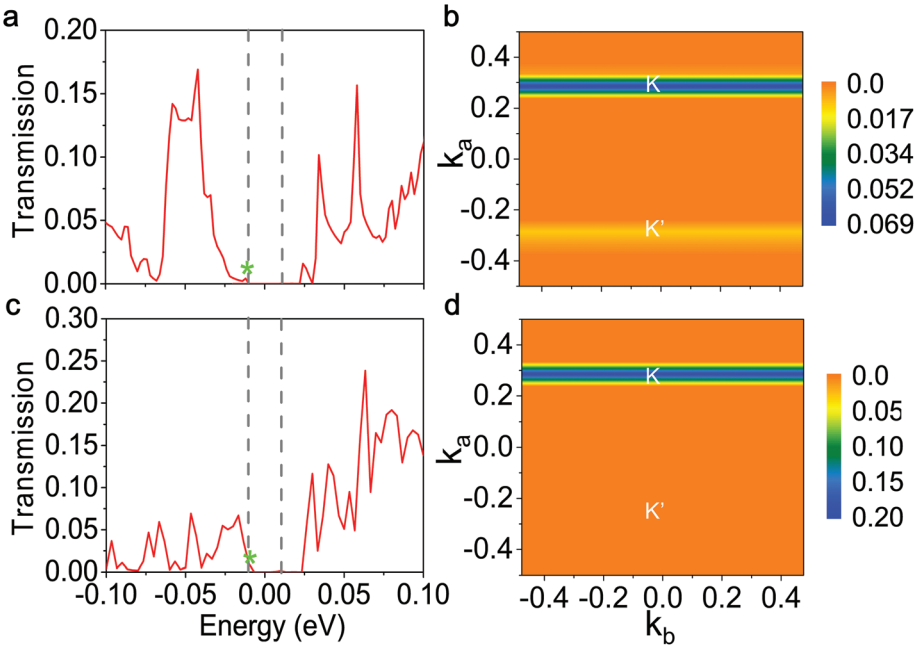

Fig. 5 Transport properties of the valleytronic devices based on the monolayer $VAgP_2Se_6$ (a) Transmission spectrum of the valley pseudospin field effect transistor under V_{ds} = 0.02 V and V_g = 0 V. (b) *k*-Resolved transmission coefficient of the state with the energy of −10 meV, which is indexed by the green star in (b). The plotted transmission state corresponds to the point indexed by the green star in (a). (c) Transmission spectrum under V_{ds} = 0.02 V and V_g = −0.5 V. (d) *k*-Resolved transmission coefficient of the state with the energy of E = −10 meV, which is indexed by the green star in (c). SOC is included here. The dashed lines represent the chemical potentials of the left and right electrodes. The transmission spectra in the vicinity of the Fermi level are fully spin polarized.

to the transmission spectrum shown in Fig. 5, the contribution to the current is mainly from electrons around E = −10 meV. The valley polarized transmission coefficient is ξ = 74% at this energy. Thus, the current is valley-polarized with an estimated polarization of $\zeta \approx 74\%$. If a suitable gate voltage is applied, the bias window covers the CBM or VBM of one of the valleys and excludes the CBM and VBM of the other valley. The valley transmission wave functions spread over the whole channel in the real space. Electrons (holes) are accelerated and transmit, resulting in a significantly enhanced valley current and setting the device in an on-state. An on-state current of 1.19 μA μm^{-1} is obtained under a gate voltage of −0.5 V, corresponding to a large current on/off ratio of 6.31×10^3. The current has a nearly complete valley-polarization in the low energy limit in terms of a valley polarization of the transmission coefficient of ξ = 100% at E = −10 meV, as shown in Fig. 5(d). Although the difference between the on-state and off-state valley current could be as large as several orders of magnitude, an improper doping approach, as well as channel lengths, gate voltages and bias voltages can degrade valley polarization of the on-state current. It is interesting that the transmission of the valley current exhibits the dependency on the magnetization directions. According to Boltzmann statistics, the valley Zeeman-type splitting of 15 meV (PBE)/35 meV (HSE) can bear a temperature of 170 K/400 K, which suggests that the VPFFTs can work effectively below 170 K or even at room temperature.

If the left and right electrodes are doped with holes and electrons, respectively, the device becomes a valley pseudospin tunneling field effect transistor (VPTFET), which is shown in Fig. 6(a). Carriers on the band extrema can transmit in the channel, and circularly polarized light can be emitted in the

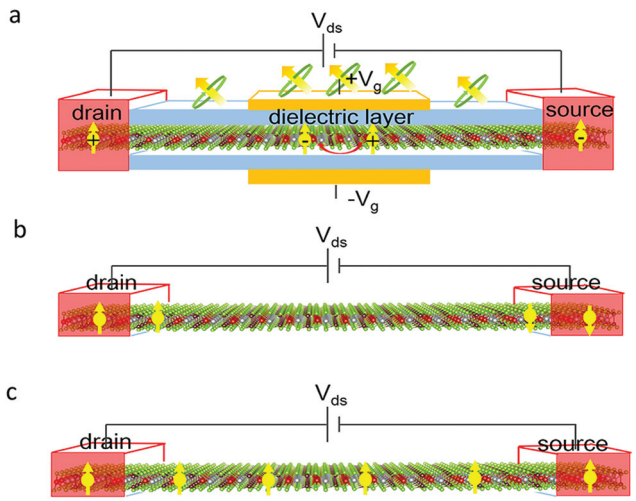

Fig. 6 (a) Schematic of the valley pseudospin tunneling field effect transistor. The plus and minus signs represent holes and electrons, respectively. Arrows in the circles represent the circularly polarized radiation, and the double arrow illustrates the combination of holes and electrons. (b and c) Schematic of valley pseudospin valves with antiparallel and parallel valley pseudospins. Arrows on the balls index the possible configurations of the valley pseudospins.

channel after inter-band recombination. By careful fabrication of a cascade structure, the quantum cascade radiation can be realized, resulting in a circularly polarized cascade laser.[38] As far as we know, the circularly-polarized-light source has rarely been reported in two-dimensional crystals. When the magnetization is reversed, the other valley is mainly transmitted, and the valley current is reversed. If the spins of the source and drain electrodes are opposite to each other, valley pseudospins are opposite at the source and drain electrodes, and the valley current is small (see Fig. 6(b)). When the spins of the source and drain electrodes are parallel, valley pseudospins are the same, and the valley current can be large (see Fig. 6(c)). Thus, a valley pseudospin valve can be designed by controlling the magnetization of the electrodes. Although the FET and VPFET seem the same in device architecture, our transistors are distinguished from previous FETs by an advantage of chirality, which is characterized by Berry curvature and optical helicity. The transmitted valleys can be detected by their chirality using circularly polarized luminescence or magneto-optical Kerr rotation.[34,39]

Generally, the calculated band structures involved in transition metal atoms are dependent on the on-site Coulomb repulsion (Hubbard U). Here the Hubbard U is self-consistently determined as 0 using Quantum Espresso packages.[40,41] The Hubbard term is $Un_{i,\uparrow}n_{i,\uparrow}$, which describes an interaction between spin-up and spin-down electrons. Near the Fermi level, the quantum states consist mainly of five spin-up d-orbitals in our systems, and thus U is determined to be 0. Therefore, our calculated results associated with the valley Zeeman-type splitting and valleytronic devices are reasonable. To further confirm our calculations, we checked our band structure with the method of HSE06 (see Fig. 2(f)). In the HSE06 band structure, the conduction bands are lifted up, and the two valence bands near the Fermi level are pushed down. The bandgap is widened to a value of 1.65 eV. Similar results have been reported in previous work.[42,43] The bandgap difference between the HSE06 and PBE results tends to become larger as the dimension decreases.[44] Compared with the PBE results, the band edges really change, since the bandgap is widened. Fortunately, valley Zeeman splitting is maintained. The two valence bands near the Fermi level are slightly mixed with deep bands projected on spin-down states. However, the main character of spin polarization remains, especially in the vicinity of the Fermi level. Due to the spin character and spin-orbital coupling, our main results of valley Zeeman-type splitting are valid. The bandgap difference increases to 35 meV between the two valleys. In the HSE06 band structure, the maximum of the valence band moves to the Γ point, but the two valleys survive. Since the Berry curvature and circular polarization at the Γ point are zero, the valley-dependent properties are nearly intact, especially the optical properties.

Methodology

Calculations of electrostatic and optical properties here are performed using the Vienna *ab initio* simulation package in the framework of the projector augmented waves.[45,46] The cutoff energy is set as 520 eV, and a vacuum space larger than 20 Å is applied to ensure decoupling periodic images. The generalized gradient approximation (GGA) of the Perdew–Burke–Ernzerhof[47] form is adopted to describe the exchange and correlation interaction. The quasi-Newton algorithm is used to relax the atoms when the crystal structure is close to the local minima of free energy. All the atoms are relaxed until the force on every atom is smaller than 0.01 eV $Å^{-1}$ using a Γ-centered $9 \times 7 \times 1$ k-point mesh.

All the converged and rigorous predictions of the valley transports are completed using a parameter-free first-principles method, which is different from the ideal concept of devices in previous studies. The device is simulated based on a model of the gated two-probe FET using nonequilibrium Green's function approach coupled with the density functional theory, which is implemented in the ATK 2016 package.[48–50] In the package, the gates and dielectric region are included during self-consistently solving the Poisson's and Kohn–Sham's equations by introducing the boundary conditions. Atomic orbital basis sets and SG15 pseudo potential are used, and the SOC is included. A Γ-centered $21 \times 1 \times 75$ k-point mesh is implemented for both the central region and electrodes. Doped ML $VAgP_2Se_6$ is used as an electrode.

Conclusions

In summary, it was found that the valleys are spontaneously nondegenerate in ML $VAgP_2Se_6$ due to the ferromagnetic ordering and SOC. The Zeeman-type valley splitting is a long-sought property due to its vital importance in valleytronic devices. Considering the optical selection rule and Zeeman-type valley splitting, a long-sought photonic chirality filter and a circularly polarized electron laser are designed using ML $VAgP_2Se_6$. Based on the valley splitting, we design a VPFET, which is another member of the transistor family. All work here, especially the simulation of devices, is completed using first-principles calculations in a stable monolayer semiconductor and thus it is possible to be realized by experimental technology in the near future. Our work may open an avenue towards valleytronic devices by the applications of spintronic concepts.

Conflicts of interest

The authors declare no competing interest.

Acknowledgements

This work was supported by the National Key Research and Development Program of China (No. 2017YFA02006303, 2017YFA0401502, 2016YFB0700901, 2017YFA0403701, and 2013CB93260), the Natural Science Foundation of China (Projects No. 51731001, 11674005, 11204110, 51371009, 51171001 and 11674132), the Foundation of He'nan Educational Committee (Grant No. 17A430026) and the National Materials Genome Project (2016YFB0700600). MHY

acknowledges the support from the Natural Science Foundation of Guangdong Province (2017B030308003) and the Guangdong Innovative and Entrepreneurial Research Team Program (2016ZT06D348), and the Science Technology and Innovation Commission of Shenzhen Municipality (ZDSYS20170303165926217 and JCYJ20170412152620376).

References

1 K. F. Mak, K. L. McGill, J. Park and P. L. McEuen, *Science*, 2014, **344**, 1489–1492.
2 D. Xiao, W. Yao and Q. Niu, *Phys. Rev. Lett.*, 2007, **99**, 236809.
3 Z. Song, R. Quhe, S. Liu, Y. Li, J. Feng, Y. Yang, J. Lu and J. Yang, *Sci. Rep.*, 2015, **5**, 13906.
4 M. B. Lundeberg and J. A. Folk, *Science*, 2014, **346**, 422–423.
5 T. Cao, G. Wang, W. Han, H. Ye, C. Zhu, J. Shi, Q. Niu, P. Tan, E. Wang and B. Liu, *Nat. Commun.*, 2012, **3**, 887.
6 H. Zeng, J. Dai, W. Yao, D. Xiao and X. Cui, *Nat. Nanotechnol.*, 2012, **7**, 490–493.
7 K. F. Mak, K. He, J. Shan and T. F. Heinz, *Nat. Nanotechnol.*, 2012, **7**, 494–498.
8 J. Xin, Y. Tang, Y. Liu, X. Zhao, H. Pan and T. Zhu, *NPJ Quantum Mater.*, 2018, **3**, 9.
9 C. Mai, A. Barrette, Y. Yu, Y. G. Semenov, K. W. Kim, L. Cao and K. Gundogdu, *Nano Lett.*, 2013, **14**, 202–206.
10 Z. Zhu, A. Collaudin, B. Fauqué, W. Kang and K. Behnia, *Nat. Phys.*, 2012, **8**, 89–94.
11 N. Nagaosa, J. Sinova, S. Onoda, A. MacDonald and N. Ong, *Rev. Mod. Phys.*, 2010, **82**, 1539.
12 F. Zhang, J. Jung, G. A. Fiete, Q. Niu and A. H. MacDonald, *Phys. Rev. Lett.*, 2011, **106**, 156801.
13 E. J. Sie, J. W. McIver, Y.-H. Lee, L. Fu, J. Kong and N. Gedik, *Nat. Mater.*, 2015, **14**, 290–294.
14 C. Zhao, T. Norden, P. Zhang, P. Zhao, Y. Cheng, F. Sun, J. P. Parry, P. Taheri, J. Wang and Y. Yang, *Nat. Nanotechnol.*, 2017, **12**, 757–762.
15 Z. Wang, J. Shan and K. F. Mak, *Nat. Nanotechnol.*, 2016, **12**, 144–149.
16 G. Aivazian, Z. Gong, A. M. Jones, R.-L. Chu, J. Yan, D. G. Mandrus, C. Zhang, D. Cobden, W. Yao and X. Xu, *Nat. Phys.*, 2015, **11**, 148–152.
17 N. Singh and U. Schwingenschlögl, *Adv. Mater.*, 2017, **29**, 1600970.
18 Y. Cheng, Q. Zhang and U. Schwingenschlögl, *Phys. Rev. B: Condens. Matter Mater. Phys.*, 2014, **89**, 155429.
19 D. Xiao, G.-B. Liu, W. Feng, X. Xu and W. Yao, *Phys. Rev. Lett.*, 2012, **108**, 196802.
20 W.-Y. Tong, S.-J. Gong, X. Wan and C.-G. Duan, *Nat. Commun.*, 2016, **7**, 13612.
21 W.-Y. Tong and C.-G. Duan, *NPJ Quantum Mater.*, 2017, **2**, 47.
22 G. Ouvrard and R. Brec, *Mater. Res. Bull.*, 1988, **23**, 1199–1209.
23 N. Sivadas, M. W. Daniels, R. H. Swendsen, S. Okamoto and D. Xiao, *Phys. Rev. B: Condens. Matter Mater. Phys.*, 2015, **91**, 235425.
24 X. Li and J. Yang, *J. Mater. Chem. C*, 2014, **2**, 7071–7076.
25 H. Wang, F. Fan, S. Zhu and H. Wu, *EPL*, 2016, **114**, 47001.
26 H. L. Zhuang, Y. Xie, P. Kent and P. Ganesh, *Phys. Rev. B: Condens. Matter Mater. Phys.*, 2015, **92**, 035407.
27 L. Casto, A. Clune, M. Yokosuk, J. Musfeldt, T. Williams, H. Zhuang, M.-W. Lin, K. Xiao, R. Hennig and B. Sales, *APL Mater.*, 2015, **3**, 041515.
28 P. Serena, N. Garci and A. Levanyuk, *Phys. Rev. B: Condens. Matter Mater. Phys.*, 1993, **47**, 5027.
29 B. Huang, G. Clark, E. Navarro-Moratalla, D. R. Klein, R. Cheng, K. L. Seyler, D. Zhong, E. Schmidgall, M. A. McGuire and D. H. Cobden, *Nature*, 2017, **546**, 270–273.
30 C. Gong, L. Li, Z. Li, H. Ji, A. Stern, Y. Xia, T. Cao, W. Bao, C. Wang and Y. Wang, *Nature*, 2017, **546**, 265–269.
31 H. Pan, Z. Li, C.-C. Liu, G. Zhu, Z. Qiao and Y. Yao, *Phys. Rev. Lett.*, 2014, **112**, 106802.
32 X. Kou, Y. Fan, M. Lang, P. Upadhyaya and K. L. Wang, *Solid State Commun.*, 2015, **215**, 34–53.
33 R. Wallauer, J. Reimann, N. Armbrust, J. Güdde and U. Höfer, *Appl. Phys. Lett.*, 2016, **109**, 162102.
34 X. Song, S. Xie, K. Kang, J. Park and V. Sih, *Nano Lett.*, 2016, **16**, 5010–5014.
35 Z. Song, Z. Li, H. Wang, X. Bai, W. Wang, H. Du, S. Liu, C. Wang, J. Han and J. Yang, *Nano Lett.*, 2017, **17**, 2079–2087.
36 S. B. Desai, S. R. Madhvapathy, A. B. Sachid, J. P. Llinas, Q. Wang, G. H. Ahn, G. Pitner, M. J. Kim, J. Bokor and C. Hu, *Science*, 2016, **354**, 99–102.
37 C. Qiu, Z. Zhang, M. Xiao, Y. Yang, D. Zhong and L. M. Peng, *Science*, 2017, **355**, 271.
38 J. Faist, F. Capasso, D. L. Sivco, C. Sirtori, A. L. Hutchinson and A. Y. Cho, *Science*, 1994, **264**, 553–555.
39 J. Huang, T. B. Hoang, T. Ming, J. Kong and M. H. Mikkelsen, *Phys. Rev. B*, 2017, **95**, 075428.
40 H. J. Kulik, M. Cococcioni, D. A. Scherlis and N. Marzari, *Phys. Rev. Lett.*, 2006, **97**, 103001.
41 M. Cococcioni and S. De Gironcoli, *Phys. Rev. B: Condens. Matter Mater. Phys.*, 2005, **71**, 035105.
42 J. Uddin, J. E. Peralta and G. E. Scuseria, *Phys. Rev. B: Condens. Matter Mater. Phys.*, 2005, **71**, 155112.
43 J. A. Kurzman, M.-S. Miao and R. Seshadri, *J. Phys.: Condens. Matter*, 2011, **23**, 465501.
44 D. Liang, R. Quhe, Y. Chen, L. Wu, Q. Wang, P. Guan, S. Wang and P. Lu, *RSC Adv.*, 2017, **7**, 42455–42461.
45 G. Kresse and J. Hafner, *Phys. Rev. B: Condens. Matter Mater. Phys.*, 1993, **47**, 558.
46 G. Kresse and J. Furthmüller, *Phys. Rev. B: Condens. Matter Mater. Phys.*, 1996, **54**, 11169.
47 J. P. Perdew, K. Burke and M. Ernzerhof, *Phys. Rev. Lett.*, 1996, **77**, 3865.
48 J. Taylor, H. Guo and J. Wang, *Phys. Rev. B: Condens. Matter Mater. Phys.*, 2001, **63**, 245407.
49 M. Brandbyge, J.-L. Mozos, P. Ordejón, J. Taylor and K. Stokbro, *Phys. Rev. B: Condens. Matter Mater. Phys.*, 2002, **65**, 165401.
50 *Atomistix ToolKit 2016*, QuantumWise A/S, Copenhagen, Denmark, 2016.